Report on the January 28, 2020 Cayman Though earthquake as imaged from regional GPS measurements

Seismotectonic context

On January 28, 2020, at 19h10 UT a shallow Mw7.8 earthquake struck the boundary between the Caribbean and North American plates in the Cuba-Jamaica area. The earthquake likely ruptured the Oriente fault, a major left-lateral strike-slip fault that separates the shallow Cayman Ridge to the north from the deep (5000-7000 m) Cayman Through to the south.
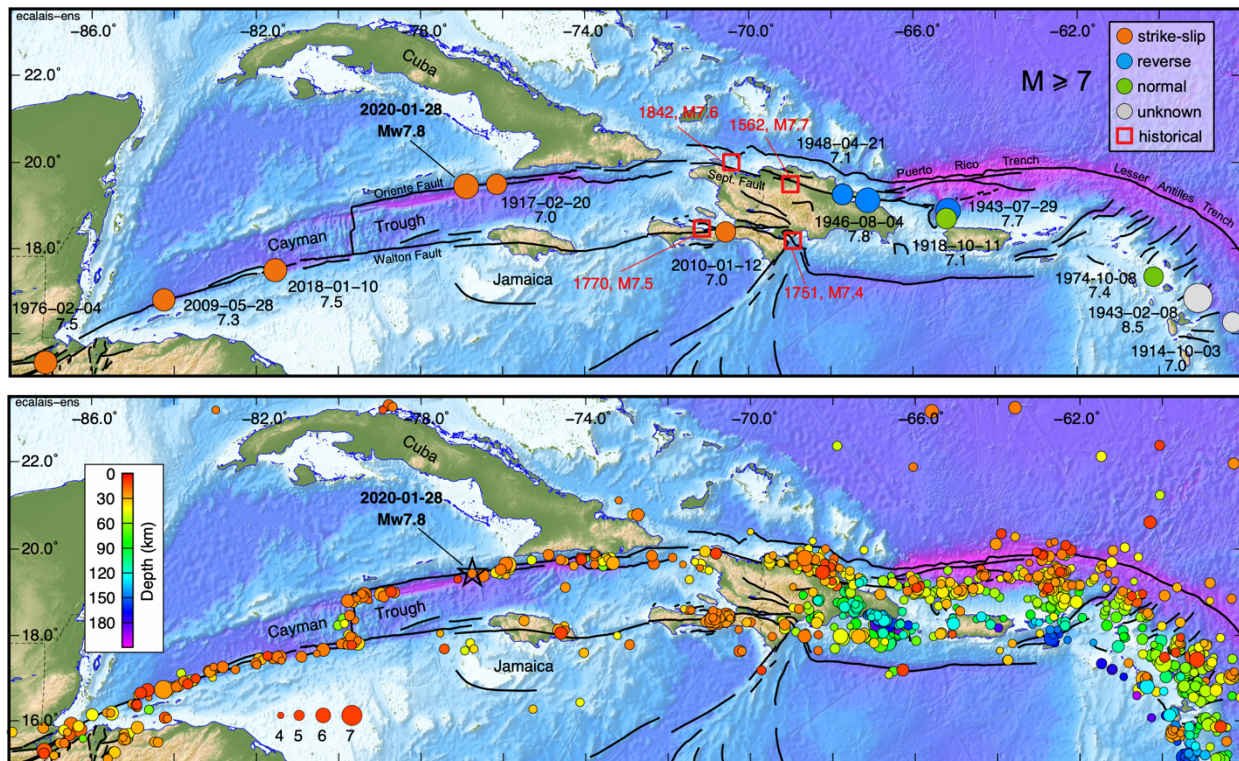

Figure 1. Top: Compilation of earthquakes with magnitude greater than or equal to 7 along the northern Caribbean plate boundary. Sources used: ISG GEM catalog (2019), tenBrink et al. (2011), Bakun et al. (2012), Stein et al. (1982), Doser et al. (2005), Hough (201). Bottom: Tectonic context of the 01/28/2020 earthquake. The epicenter is shown with a black star. Colored circles show the location of M>4 earthquakes in the region from the ISC-EHB database, color-coded as a function of depth. Black lines show major active faults.

This earthquake is the largest strike-slip event of the instrumental seismology era along the northern Caribbean plate boundary (Figure 1), ranking right after the Ms7.5 event that struck Guatemala on February 4th 1976 along the Motagua fault section of the plate boundary (Plafker, 1976). Historical events with similar magnitude and source mechanism have been described further east along the same fault system in 1842 in northern Haiti and 1562 in the northern Dominican Republic (Scherer, 1912; Man et al., 1998; Prentice et al., 2003; ten Brink et al., 2011).

This event is similar in magnitude to two large historical earthquakes that likely ruptured the eastward continuation of the Oriente fault in Hispaniola, where it is called the "Septentrional

fault". ten Brink et al. (2011) quote a December 2, 1562, event in the Cibao valley of the Dominican Republic at MI7.7, and the May 7, 1842, event of northern Haiti at MI=7.6 (intensity magnitudes). It is much larger than the three largest known earthquakes that struck southern Cuba in 1766, 1852, and 1932, with magnitudes of 6.8, 6.4, and 6.75, respectively (Cotilla and Cordoba, 2010) — although previous authors proposed larger magnitudes (M7.5 and M7.3 for the 1766 and 1852 events, respectively, according to Alvarez et al., 2001).

Although the January 28, 2020, Cayman Trough earthquake was widely felt in the region - there were reports of shaking all the way to Florida - it fortunately caused limited damage. No fatalities were reported, only a few poorly-built houses where affected in the Granma province of Cuba. Had this earthquake occurred further east along the more populated segments of the Oriente-Septentrional fault system, damage and fatalities could have been very significant.
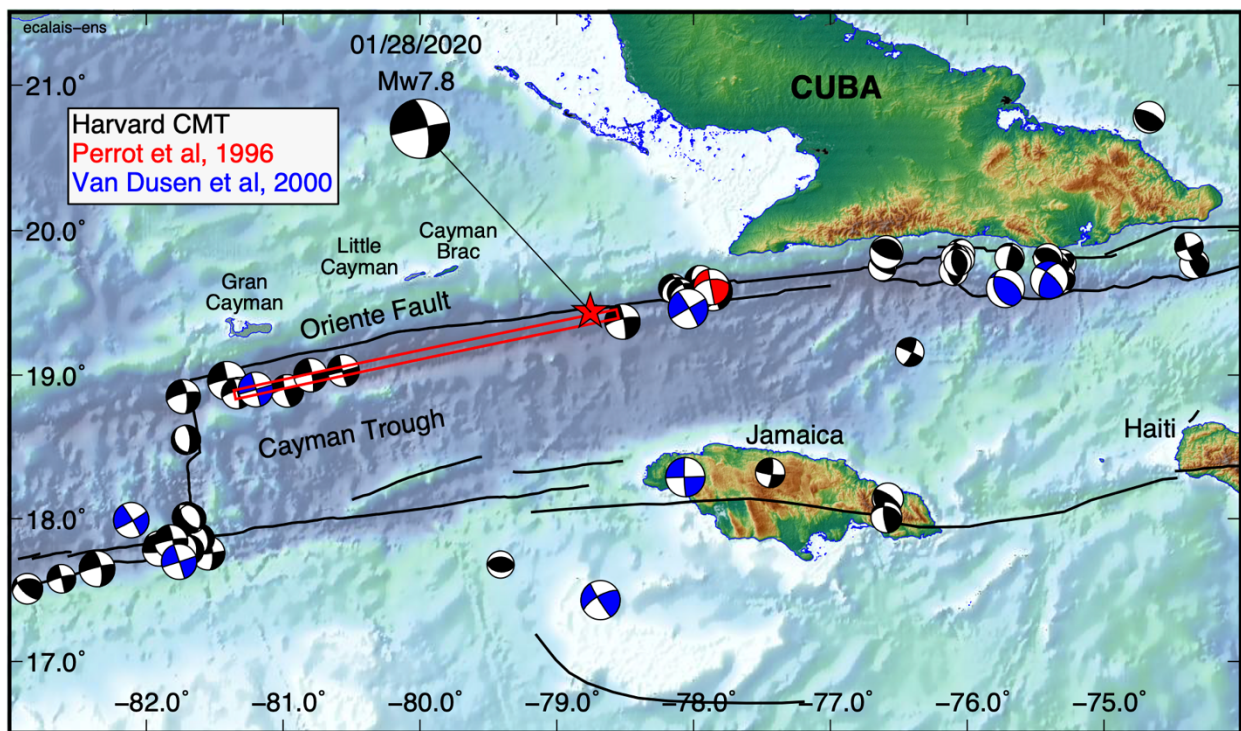

Figure 2. Focal mechanism of the January 28, 2020, Mw7.8 Cayman Through earthquake in its seismo-tectonic context. The focal mechanism and epicenter (red star) displayed are from the USGS. The red rectangle shows the finite fault rupture as modeled by B. Delouis (see below).

The source mechanism for this earthquake has been computed by several centers (Figure 2). Its moment magnitude is calculated at 7.8 by Géoscope and at 7.7 by the USGS. The event very likely ruptured the Oriente fault, a major quasi-vertical left-lateral strike-slip fault that bounds the Cayman Trough to the north. Its mechanism is consistent with known focal mechanisms along that same fault, at least from its junction with the mid-Cayman spreading center to the western tip of the Cuban Oriente (Perrot et al., 1996; Van Dusen et al., 2000; Moreno et al., 2002). Figure 1 (bottom) and Figure 2 show that the January 28, 2020, rupture filled a segment of the Oriente fault that had been devoid of significant events for at least the past ~100 years.

GPS observations

We used position time series at continuously-recording GPS stations in the northern Caribbean to determine coseismic displacements. This was performed in two different ways: 24-hour static solutions and 15-second epoch-by-epoch solutions.

24-hour solutions

We computed static solutions for 24-hour sessions (from 00:00 to 23:50 UT) using the GAMIT software, using a well-established procedure described in detail, for instance, in Symithe et al., (2015). This leads to time series of daily site positions, which we use to estimate the coseismic offset. The day of the earthquake is removed so that it does not affect the coseismic estimation, as site positions on that day contain both pre- and post-earthquake data. The estimation uses a simple least-squares solver that includes daily positions from January 1st to 31st, except at site CN16 where data is available until January 29th only. We assume no long-term site displacement over that time interval (i.e., zero velocity) and only estimate one coseismic offset per site together with its uncertainty. The static, 24-hour solutions have the advantage of providing the most precise positions but the coseismic estimation may be biased by some postseismic deformation. This is however minimized by only using 3 post-earthquake days.

The daily position time series for the month of January are shown on Figure 4 for two sites on the Cayman Islands and on Figure 4 for two sites in Cuba. The time series for all Cuban and Cayman Island sites, as well as one site in Jamaica, are provided in the appendix.
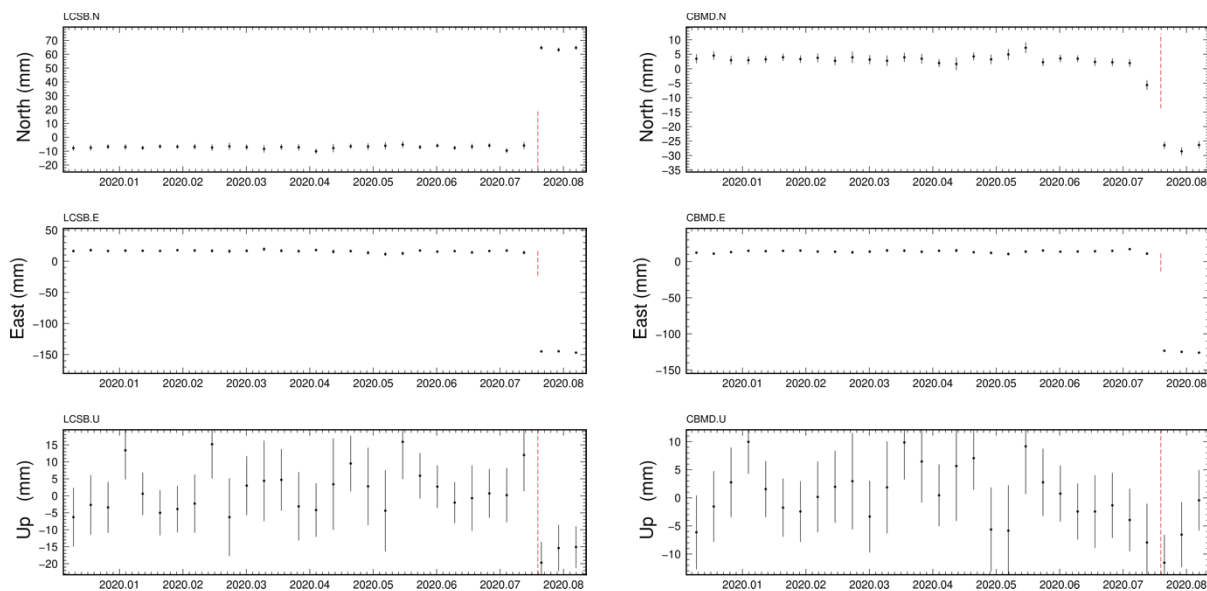

Figure 3. Daily position time series at sites LCSB (Little Cayman) and CBMD (Cayman Brac) in Cayman Islands. The red vertical dashed line shows the time of the earthquake.

Coseismic displacements are clearly visible on all components at the Cayman Islands sites (Figure 3 and Appendix), located within a few tens of kilometer of the earthquake rupture, with values reaching up to 15 cm on the east component at site LCSB. Significant coseismic displacements are also visible at site CN12 in Jamaica (see Appendix). Cayman Island sites all moved westward

while CN12 moved eastward, consistent with a mostly left-lateral strike-slip earthquake source mechanism.
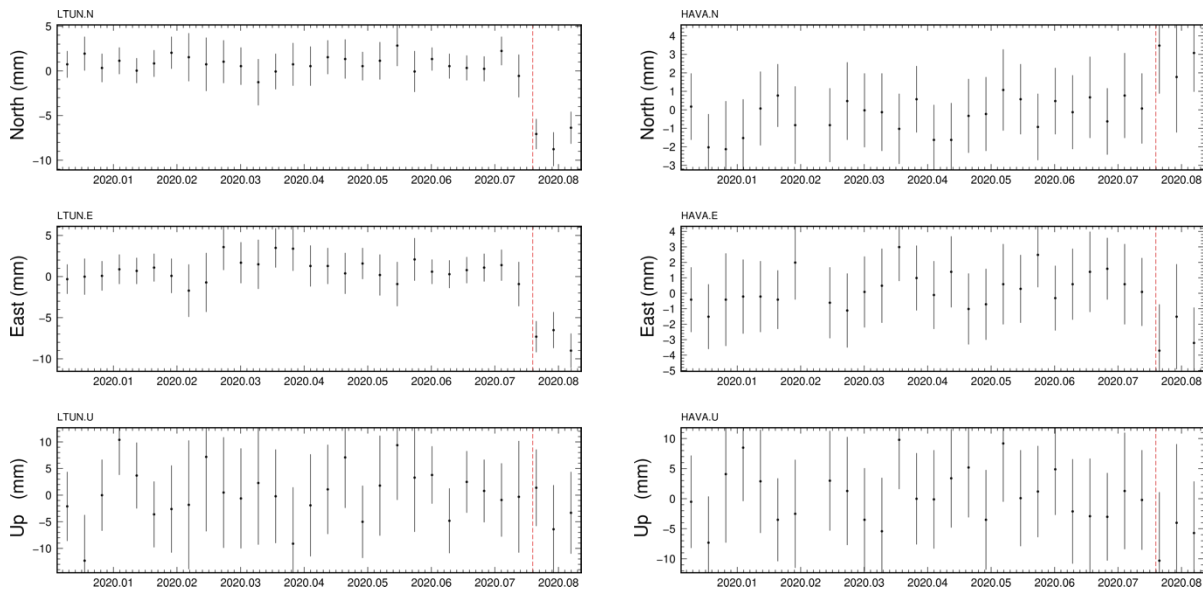

Figure 4. Daily position time series at sites LTUN (Las Tunas) and HAVA (La Habana) in Cuba. The red vertical dashed line shows the time of the earthquake.

Coseismic displacements are also visible at all Cuban sites, though with smaller values than on the Cayman Islands because of the larger distance to the earthquake source. Horizontal displacement is largest at site LTUN (Las Tunas), with 11 mm of southwestward displacement, clearly visible on Figure 4. Horizontal coseismic displacement is smaller at site HAVA (La Habana), but still quite visible on Figure 4, with 4 mm of northwestward displacement.

Epoch-by-epoch solutions

We also computed 15-second, epoch-by-epoch solutions using the TRACK software, which computes multi-site, baseline solutions. We used data from January 28. These solutions are less precise that the static, 24-hour ones, but (1) they provide an estimate of the coseismic static displacement that is unbiased by possible post-seismic deformation, (2) when coseismic displacement is sufficient and the GPS sampling rate sufficient, they can also show absolute ground displacement during earthquake dynamic shaking. Unfortunately, none of the sites in the regional vicinity of the earthquake source was recording data at periods shorter than 15 seconds, so that nothing can really be learned on the dynamic part. Ideally, continuous GPS stations would have to be sampling at a rate of at least 1 Hz, preferably even higher, in order to provide useful dynamic information.

In addition, because of the lower precision of epoch-by-epoch solutions compared to daily ones, clear coseismic displacements are visible mostly at the four Cayman Island GPS sites. The 15-second times series are shown on Figure 5.
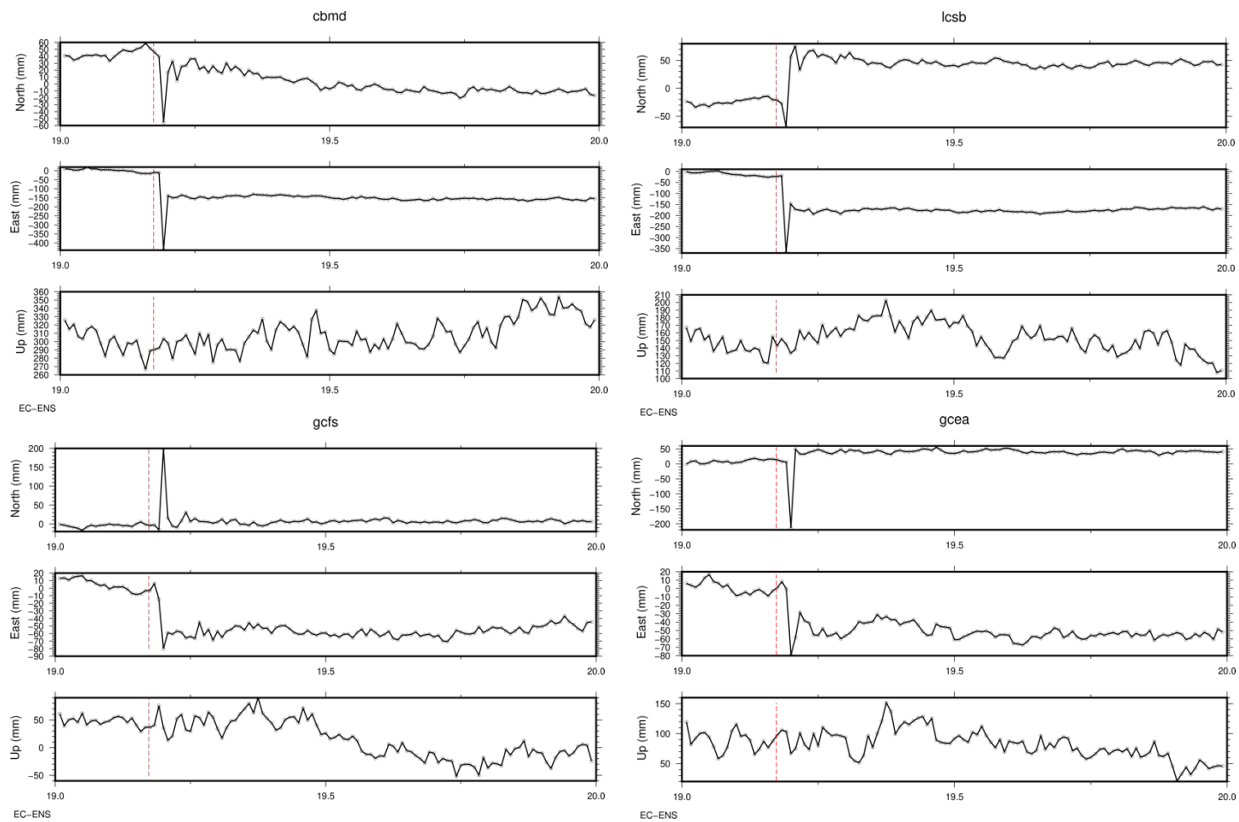
Figure 5. Epoch-by-epoch, 15-second interval, position time series at the four continuous GPS sites located on the Cayman Islands. The red dashed line shows the time of the earthquake.

The coseismic site motion is clearly visible on the horizontal components at the four sites, with an overshoot that corresponds to the aliased sampling of the dynamic ground motion (seismic waves), then a plateau that corresponds to the final, static, coseismic offset.

Coseismic GPS displacements

Coseismic displacements values in 3 dimensions are provided in the Appendix. They are clearly visible in both the 24-hour and epoch-by-epochs time series at sites in the near-field of the earthquake source on the Cayman Islands (sites GCEA, GCFS, LCSB, and CBMD). They are also visible in the 24-hour solutions at sites farther away from the source, such as CN12 in Jamaica, or at sites BYMO, LTUN, CN16, ISLA, HAVA, and CARD in Cuba. They can also be detected at sites even farther away, tough with smaller confidence, in Yucatan (Mexico) at sites TGMX and UNPM, in the Bahamas at sites CN13, CN53, and CN14, and on the islands of San Andres (SAN0) and Fresh Water Bay (CN35) in the Colombian basin.
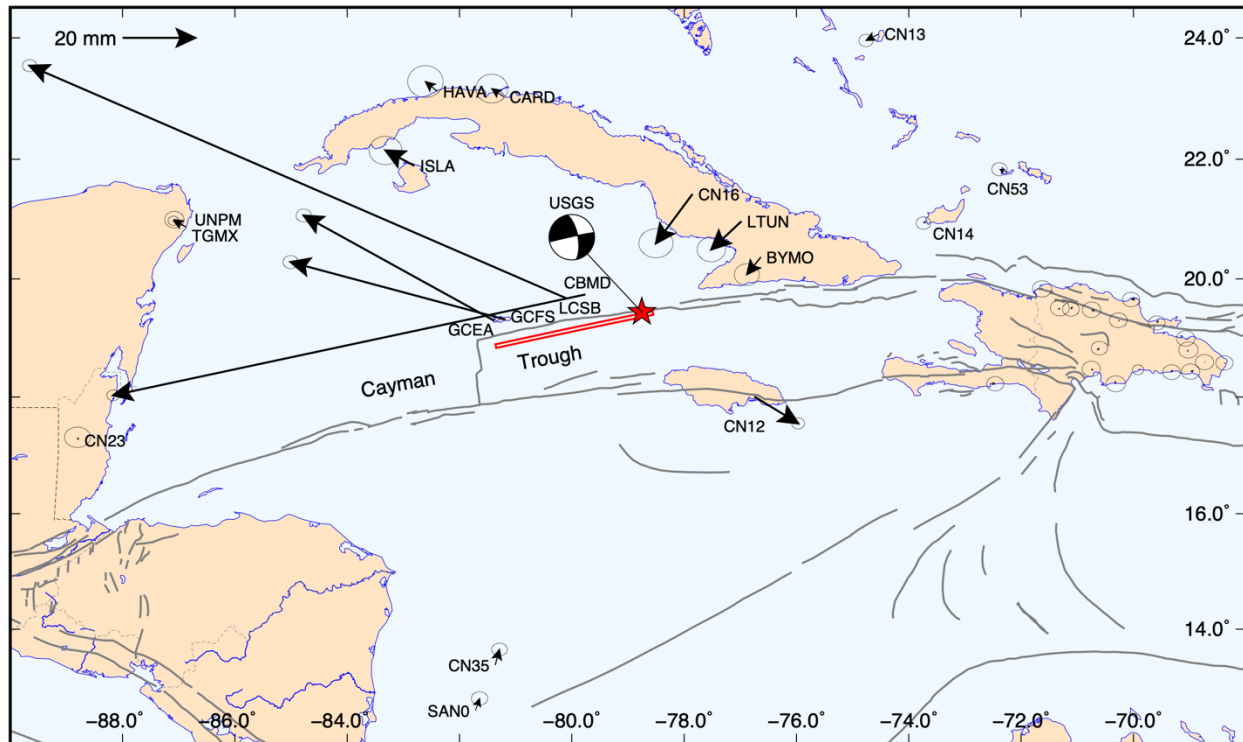
5

Figure 6. Map view of the horizontal coseismic displacements derived from daily position times series at continuous GPS sites surrounding the epicenter of the January 28, 2020, Mw7.4 Cayman Though earthquake. The focal mechanism and epicenter (red star) displayed are from the USGS. The red rectangle shows the finite fault rupture as modeled by B. Delouis (see below). Grey lines show major active faults.

In map view (Figure 6), coseismic displacements at regional GPS sites show a pattern consistent with one should expect from a mostly left-lateral strike-slip source mechanism. It is interesting to observe that coseismic displacements qualitatively consistent with such a mechanism can be observed all the way to HAVA (Cuba), CN13 (Bahamas), UNPM/TGMX (Mexico), or SAN0 (San Andres island, Colombia).

In the near-field of the rupture, sites CBMD and LCSB located at close distance to each other show significantly different horizontal coseismic displacements, an indication of slip variability along the rupture.

Preliminary finite fault models

Here we discuss two finite fault models calculated shortly after the earthquake. None of them used GPS data to constrain their solution:

- A model produced by Gavin Hayes at the USGS (Denver, Colorado), which uses 30 teleseismic broadband P waveforms, 9 broadband SH waveforms, and 44 long period surface waves selected based on data quality and azimuthal distribution. The algorithm is described in Ji et al. (2002). The calculations use a layered elastic Earth model and account for the ocean depth.
- A model produced by Bertrand Delouis at Géoazur (Nice, France), which uses 18 teleseismic broadband P and SH waveforms and the full waveform at 13 regional broadband stations within the area covered by Figure 6. Near-field stations on the

Cayman Islands were not used. The calculations use a homogeneous elastic half-space and do not account for the ocean depth.
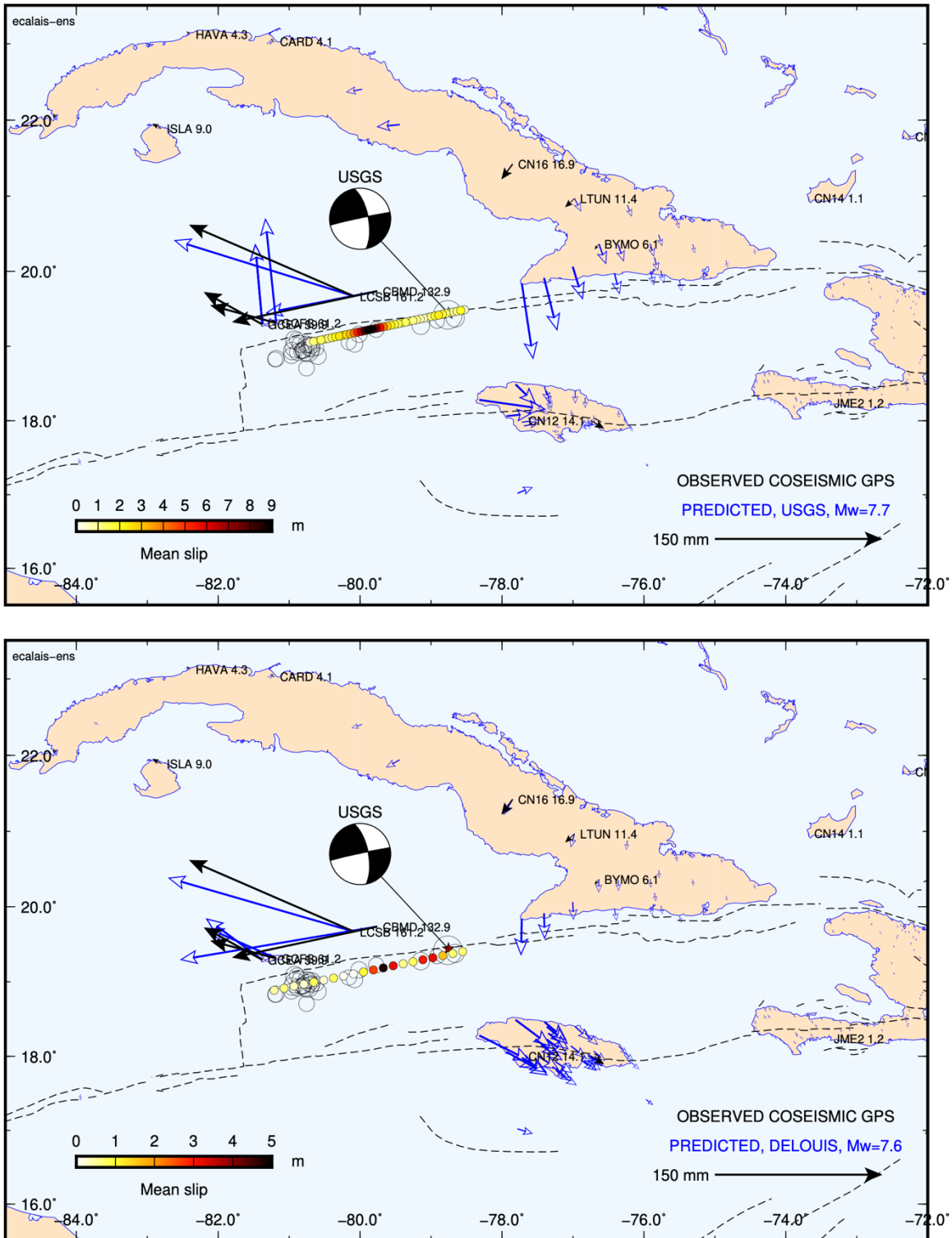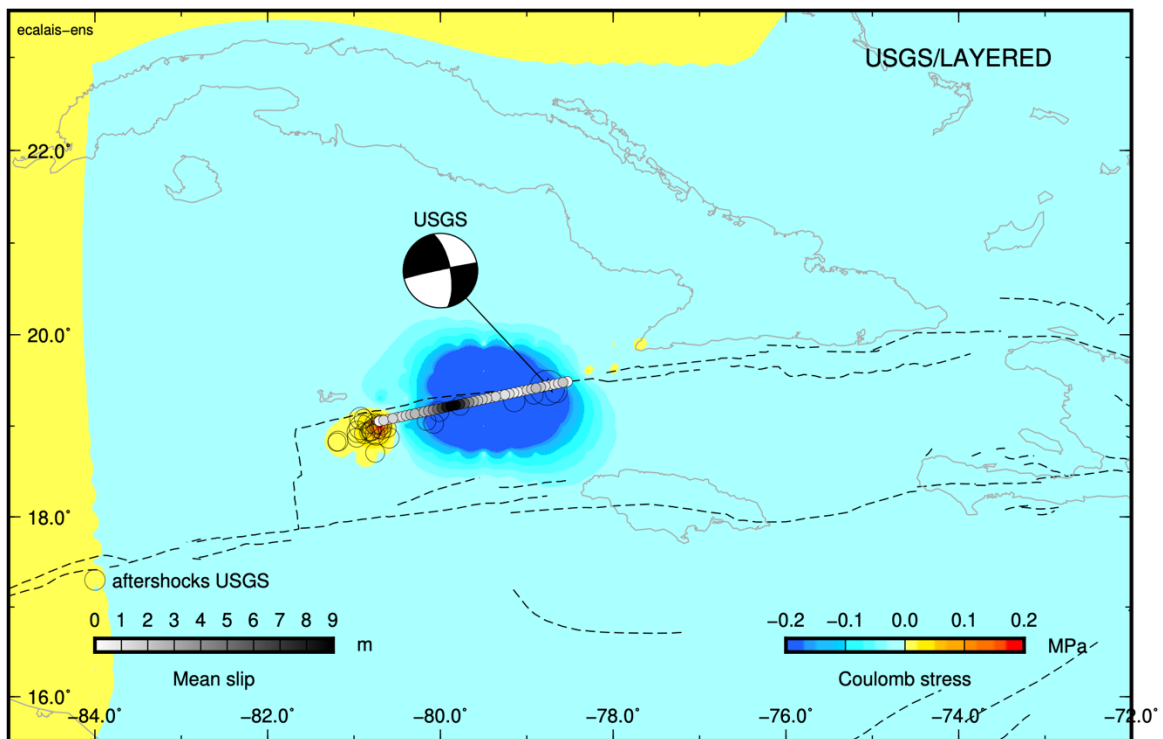

Figure 7. Comparison of two finite fault models of the January 28, 2020, Cayman Trough earthquake. Colored circles show the extent of the modeled rupture, they are color-coded as a function of the average estimated slip on a vertical profile. Black arrows

In both models: (1) the rupture follows the narrow and deep linear basin at the toe of the Cayman Ridge, (2) slip initiates close to the eastern end of the rupture and propagates westward, and (3) slip is contained within the first 20 km. Therefore, the earthquake likely rupture most of the crust, which is about 20 km thick in this region (Moreno et al., 2002).

The coseismic slip distribution and predicted horizontal coseismic displacements for the two models are shown on Figure 7. Fault slip is larger -- up to 9 m -- in the USGS model than in the Géoazur one -- up to 5 m. Both models however find roughly the same area of maximum slip just to the south of Little Cayman. Predicted horizontal coseismic displacements at the GPS sites are consistent with observations, particularly for the Géoazur model. The USGS model predictions deviate from observations on Grand Cayman, in particular. Coseismic observations at sites LTUN and BYMO in Cuba are also better predicted by the Géoazur model.

Both models predict measurable coseismic deformation at campaign sites in the Cuban Oriente and in Jamaica. This has two consequences: (1) remeasuring these sites would provide additional constrain on the finite fault source, and (2) the calculation of interseismic velocities from GPS measurements will need to account for this earthquake.
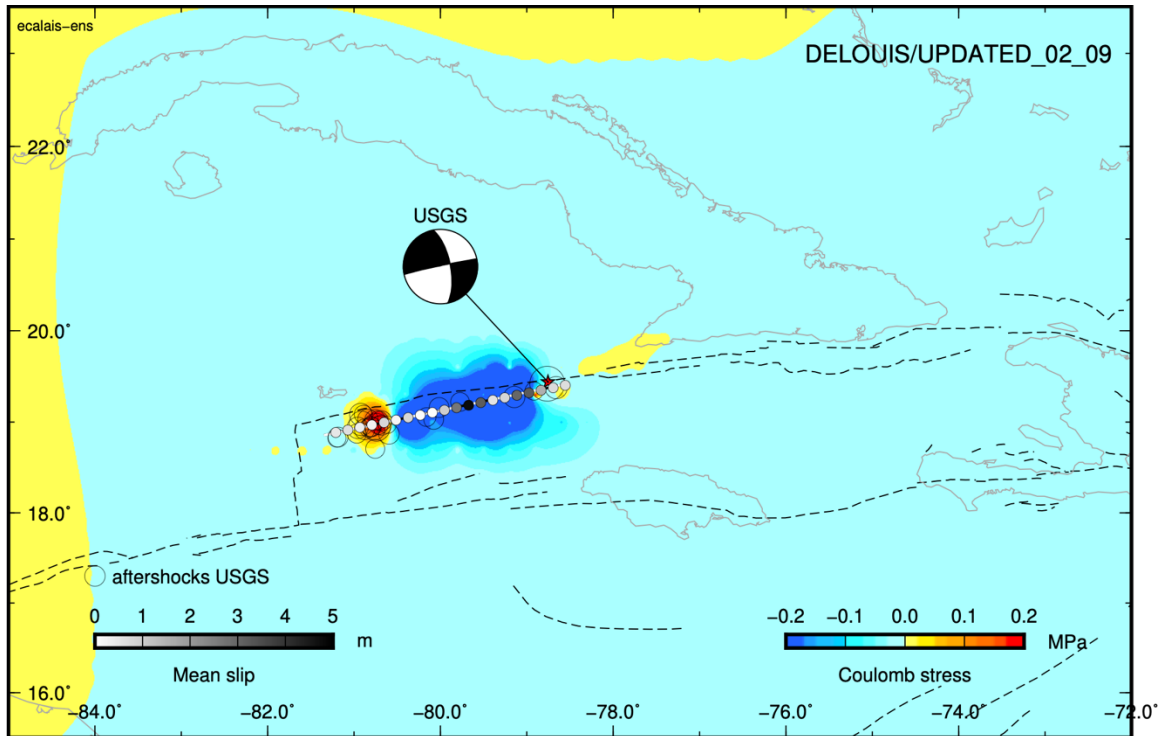
Figure 8. Coulomb stress changes predicted by the USGS (top) and Géoazur (bottom) finite fault models at a depth of 5 km for receiver faults striking N78 with pure left-lateral strike-slip motion, with a friction coefficient of 0.2. Grey circles show the extent of the modeled rupture, they are color-coded as a function of the average estimated slip on a vertical profile. Black arrows are observed horizontal coseismic displacements from GPS, blue arrows are model predictions at continuous and campaign GPS sites in the region. Open black circles show the early aftershocks (USGS). Dashed grey lines are main active faults.

Figure 8 shows the change in Coulomb failure stress (CFS) imparted by the coseismic slip distribution from the finite fault models on receiver faults striking N74 with pure left-lateral strike-slip motion. The both show the decrease in CFS along the main part of the rupture, where coseismic slip was largest, as well as a significant increase in CFS at the western end of the rupture, coinciding with a concentration of early aftershocks. It is therefore quite possible that these early aftershocks, which include a Mw6.1 event, were triggered by static coseismic stress changes.

Tsunami observations

Even though the January 28, 2020, Cayman Trough earthquake had a largely strike-slip source mechanism, it generated a small tsunami signal well recorded at tide gauges in the near-field on Grand Cayman (Georgetown) and in the far field in Yucatan (Puerto Morelos, close site UNPM on Figure 6). Peak-to-peak water height variations reach 80 cm at Georgetown and 8 cm at Puerto Morelos. In Georgetown, the first arrival is flowed by oscillation of up to +-10 cm that last for several hours, possibly the result of harbor resonance.

The cause of the tsunami remains to be fully understood, as strike-slip earthquakes are not prone to generating significant vertical seafloor coseismic displacement. One could perhaps invoke a local underwater slope instability triggered by the earthquake ground motion to explain observations at Georgetown, but this unlikely to explain why the tsunami reached the Yucatan.

These tsunami observations would very much benefit from additional tide gauge data in Cuba. Dr. Castellanos provide data from a tide gauge station near Cienfuegos, but it does not show any tsunami signal. This could mean that the tide gauge is too far from the rupture, or that there was some directivity in the generation of the tsunami since it is observed in Yucatan, at a greater distance. Alternatively, this may result from the fact that the location of the tide gauge (Cayo Loco) is inside a closed bay (Bahia de Jagua) with communication to the open sea through a very narrow channel. It could simply be that if there was a small tsunami, it got filtered out by the channel/bay system. In any case, data from the tide gauge stations in Santiago de Cuba, Cabo Cruz, Manzanillo, Santa Cruz de Sur, or Trinidad would be quite interesting to collect and investigate.
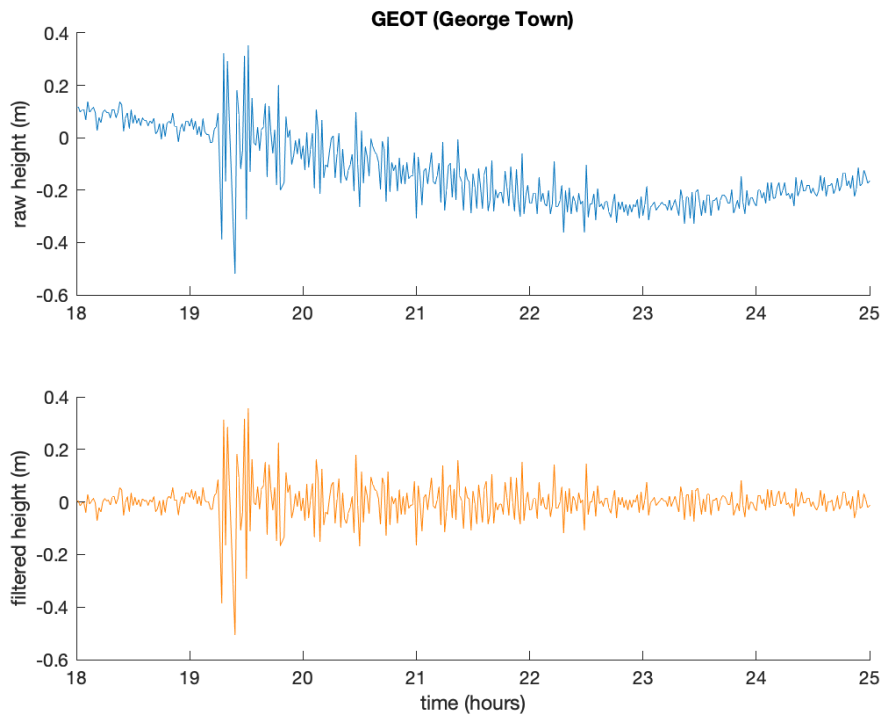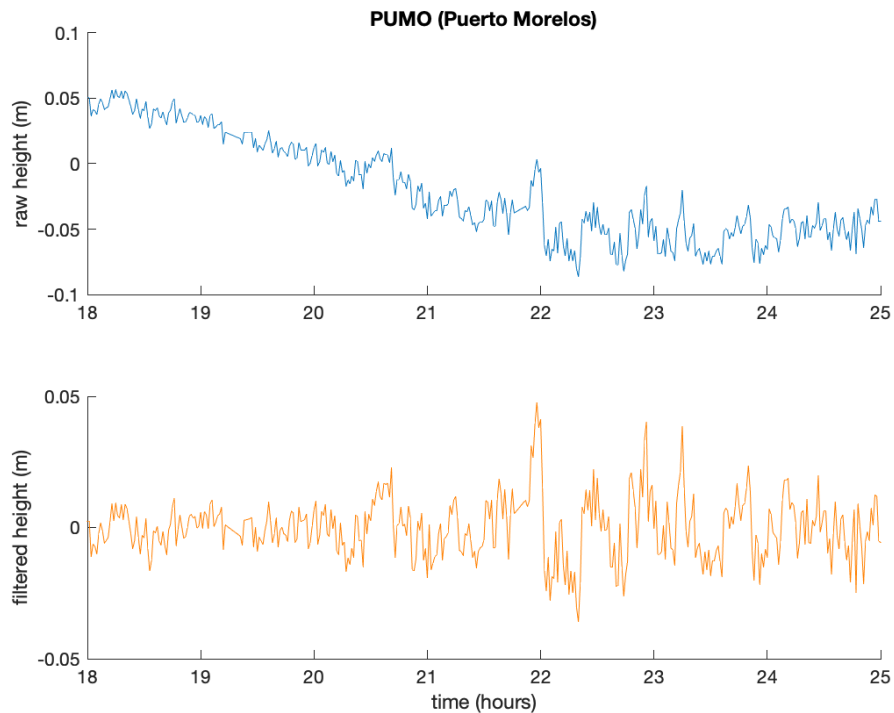
Figure 9. Tide gauge observations at Georgetown (Grand Cayman) and Puerto Morelos (Yucatan). Blue time series shows the raw data, orange show the high-pass filtered data with a cutoff frequency of 1 hour.

Conclusions

The January 28, 2020, Mw7.7 Cayman Trough earthquake was well recorded by regional continuous GPS stations, in particular in Cuba. Coseismic motion is visible in the GPS position time series all the way to La Habana (4 mm), located about 450 km from the earthquake source. Therefore, remeasuring campaign GPS sites in Cuba would provide additional constrains on the finite fault source models, which are currently calculated from seismological data only.

The two finite fault models discussed here remain to be improved to better fit the GPS observations. However, they already show that the entire Cuban territory was affected by a significant static displacement ranging from a few millimeters (4 mm were measured at La Habana) to several centimeters in the western part of the Oriente region (model predictions of 3 to 7 cm at Cabo Cruz).

This implies that the calculation of interseismic velocities from GPS measurements in Cuba (and Jamaica as well) will need to account for this earthquake, either in the form of an offset estimated from position time series, or from a coseismic offset correction from the best earthquake source model.

This coseismic deformation of the Cuban territory, although modest, may also have a consequence on the definition of the national geodetic datum. It is quite clear that all the Cuban continuous GPS stations analyzed here shifted position by up to 1 cm (site Las Tunas).

11

Acknowledgments

Eric Calais, eric.calais@ens.fr, May 3, 2020

References

Alvarez, L., G. F. Panza, F. Vaccari, and B. E. González, Modelling of Seismic Ground Motion in Santiago de Cuba City from Earthquakes in Oriente Fault Seismic Zone, Pure and Applied Geophysics, vol. 158, no. 9, pp. 1763–1782, 2001.

Bakun, W.H., C. H. Flores, and U. S. ten Brink, Significant Earthquakes on the Enriquillo Fault System, Hispaniola, 1500-2010: Implications for Seismic Hazard, Bulletin of the Seismological Society of America, vol. 102, no. 1, pp. 18–30, 2012.

DeMets, C., and M. Wiggins-Grandison, Deformation of Jamaica and motion of the Gonâve microplate from GPS and seismic data, Geophysical Journal International, vol. 168, no. 1, pp. 362–378, 2007.

Doser, D., C. Rodríguez, and Claudia Flores. Historical earthquakes of the Puerto Rico-Virgin Isalnd region. In "Active tectonic and seismic hazards of Puerto Rico, the Virgin Islands, and offshore areas", Mann, P. (ed.), pp. 103-114, 2005.

Hough, S.E., Missing great earthquakes, J. Geophys. Res. Solid Earth, vol. 118, no. 3, pp. 1098–1108, 2013.

ISG-GEM Global Instrumental Earthquake Catalogue, Version 6.0, DOI: 10.31905/D808B825 March 7, 2019.

Mann, P., F. W. Taylor, R. L. Edwards, and T. L. Ku, Actively evolving microplate formation by oblique collision and sideways motion along strike-slip faults: An example from the northeastern Caribbean plate margin, Tectonophysics, vol. 246, no. 1, pp. 1–69, 1995.

Mann, P., C. S. Prentice, G. Burr, L. R. Peña, and F. W. Taylor, Tectonic geomorphology and paleoseismology of the Septentrional fault system, Dominican Republic, in Special Paper 326: Active Strike-Slip and Collisional Tectonics of the Northern Caribbean Plate Boundary Zone, vol. 326, Geological Society of America, 1998, pp. 63-123.

Moreno, B., M. Grandison, and K. Atakan, Crustal velocity model along the southern Cuban margin: implications for the tectonic regime at an active plate boundary, Geophysical Journal International, vol. 151, pp. 632–645, 2002.

Plafker, G., Tectonic Aspects of the Guatemala Earthquake of 1976 February 1976, Science, vol. 193, no. 4259, pp. 1201–1208, 1976.

Prentice, C.S., P. Mann, L. R. Pena, and G. Burr, Slip rate and earthquake recurrence along the central Septentrional fault, North American-Caribbean plate boundary, Dominican Republic, Journal of Geophysical Research, vol. 108, no. 3, pp. 810-817, 2003.

Rodríguez M. O. C. and D. C. Barba, The August 20, 1852 earthquake in Santiago de Cuba, Russian Geology and Geophysics, vol. 51, no. 11, pp. 1227–1246, 2010.

Scherer, J., Great earthquakes in the island of Haiti, Bulletin of the Seismological Society of America, pp. 161–180, 1912.

Stein, S., J. F. Engeln, D. A. Wiens, and K. Fujita, Subduction seismicity and tectonics in the Lesser Antilles arc, J. Geophys. Res., vol. 87, no. B10, pp. 8642-8664, 1982.

Symithe, S., E. Calais, J. B. Chabalier, R. Robertson, and M. Higgins, Current block motions and strain accumulation on active faults in the Caribbean, Journal of Geophysical Research (Solid Earth), vol. 120, doi:10.1002/2014JB011779, 2015.

ten Brink, U. S., W. H. Bakun, and C. H. Flores, Historical perspective on seismic hazard to Hispaniola and the northeast Caribbean region, J. Geophys. Res., vol. 116, no. 12, pp. B12318–15, 2011.

Van Dusen, S. R. and D. I. Doser, Faulting Processes of Historic (1917–1962) M≥ 6.0 Earthquakes Along the North-central Caribbean Margin, Pure and Applied Geophysics, vol. 157, no. 5, pp. 719–736, 2000.

Appendix
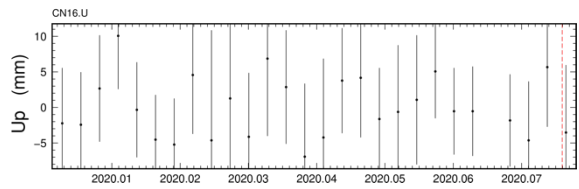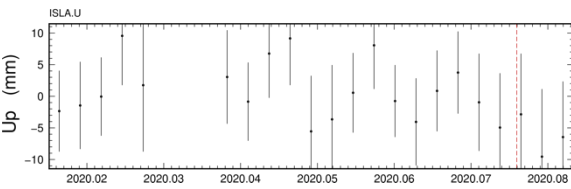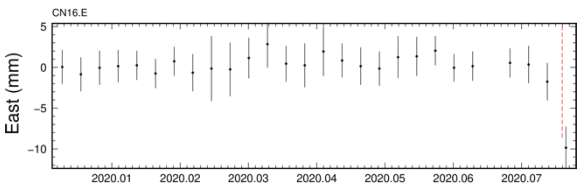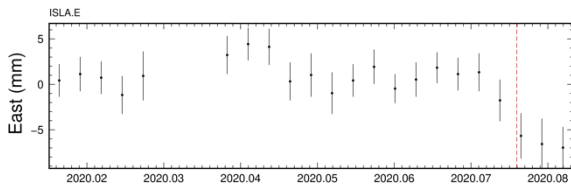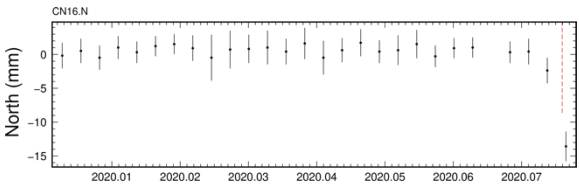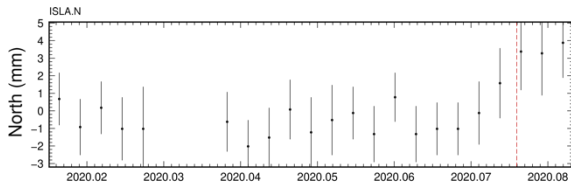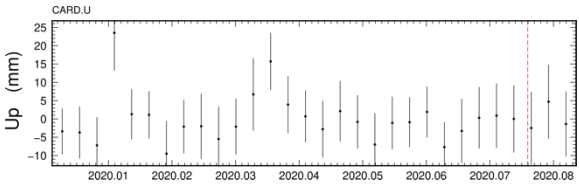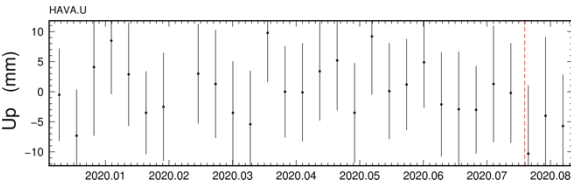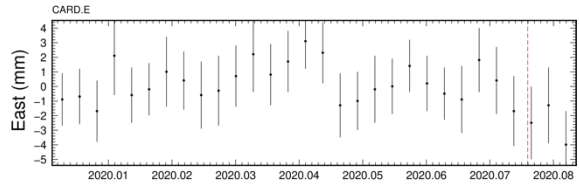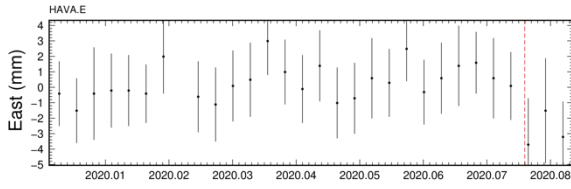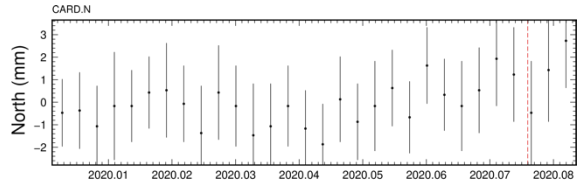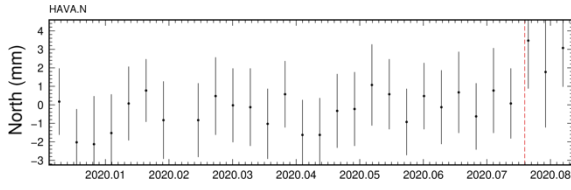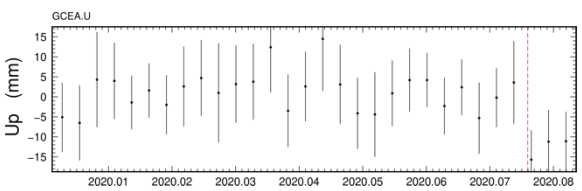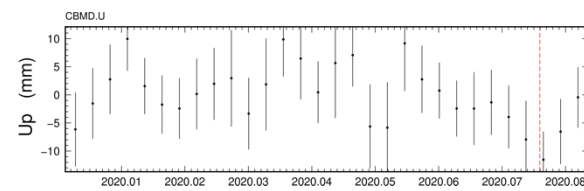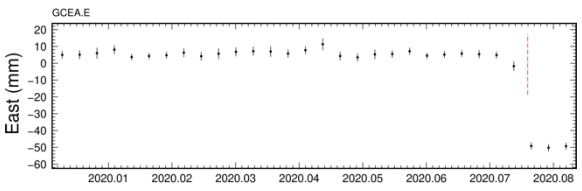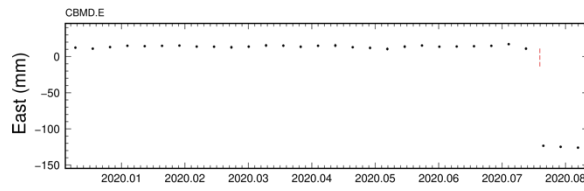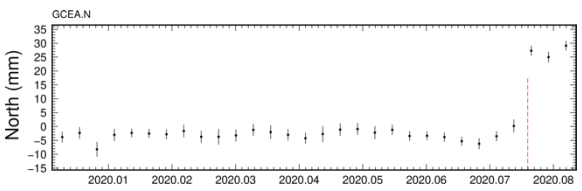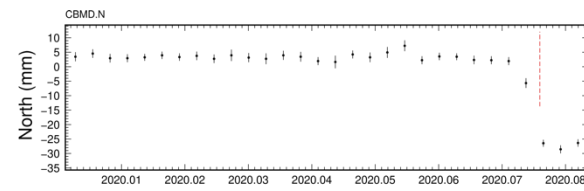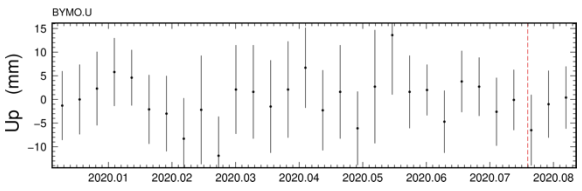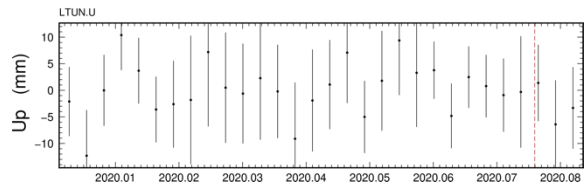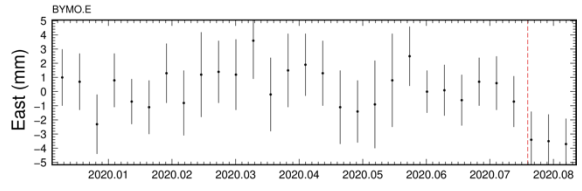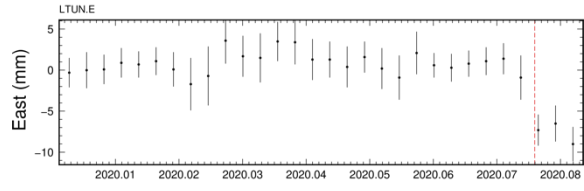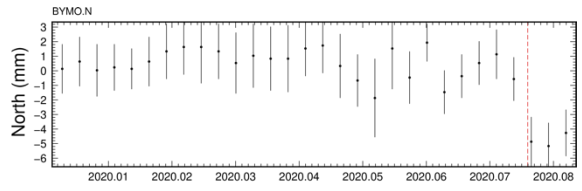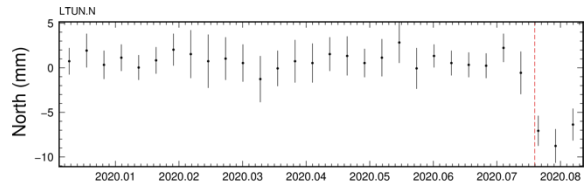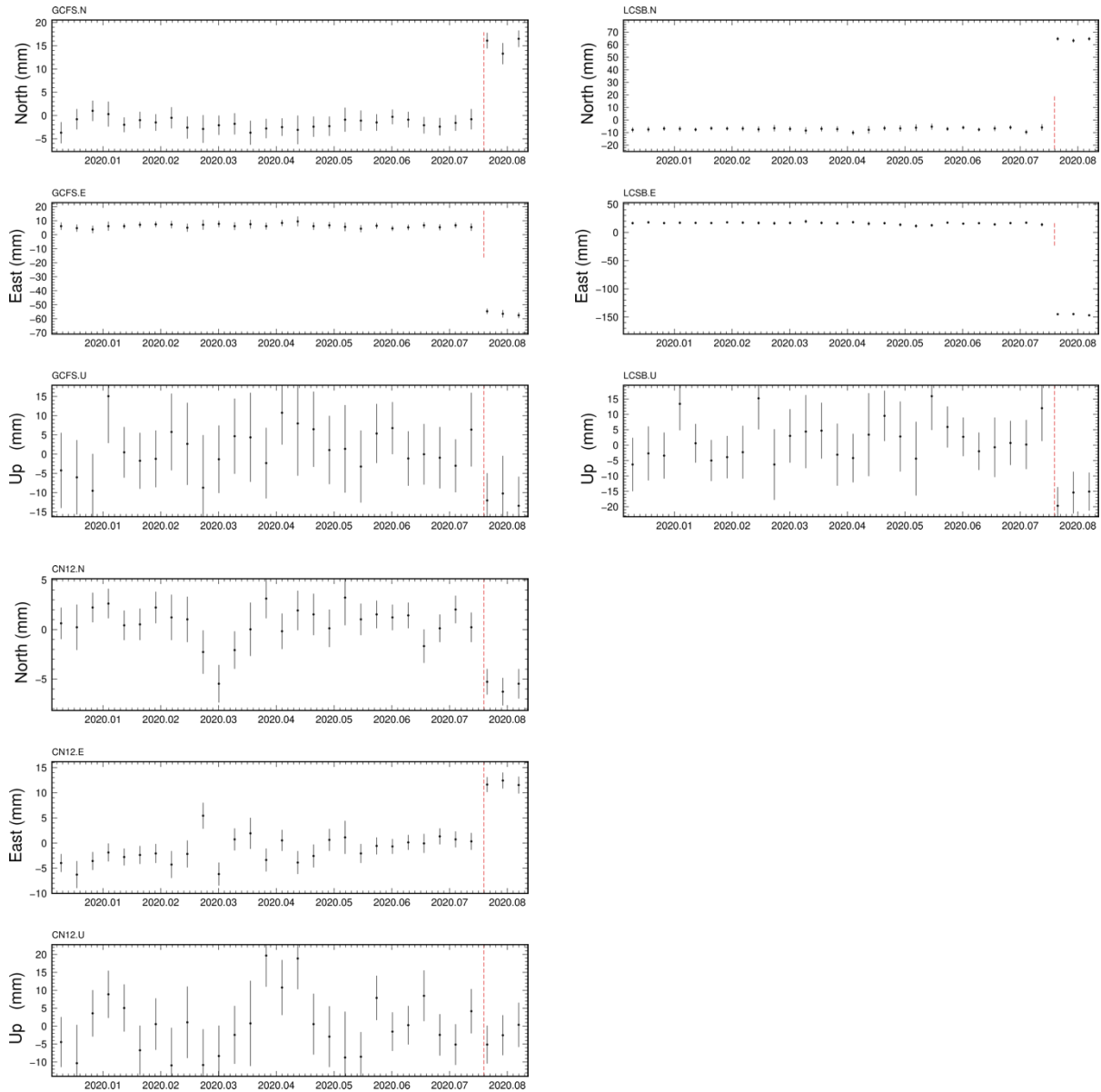
Daily position time series at continuous GPS sites on the Cayman Islands, Cuba, and Jamaica. The red dashed line indicates the time of the earthquake. The site locations can be found on Figure 6.

	Position		Displacement			Standard dev.			
SITE	Long.	Lat.	east	west	up	east	west	up	3D
LCSB	−80.082	19.668	−147.94	64.09	−14.54	0.8	0.68	2.88	161.22
CBMD	−79.758	19.738	−129.95	−27.76	−0.28	0.72	0.61	2.58	132.88
GCFS	−81.184	19.313	−59.08	15.82	−10.66	0.86	0.73	3.13	61.16
GCEA	−81.378	19.293	−52.48	28.96	−9.49	0.86	0.73	3.12	59.94
CN16	−77.850	21.422	−10.08	−13.57	−3.71	1.92	1.63	7.02	16.90
CN12	−76.749	18.450	12.04	−7.35	−3.85	0.72	0.63	2.63	14.11
LTUN	−76.979	20.968	−8.31	−7.79	−5.26	1.60	1.38	5.96	11.39
ISLA	−82.803	21.892	−7.96	4.22	−8.95	1.85	1.60	7.05	9.01
BYMO	−76.635	20.365	−3.84	−4.80	−0.58	1.41	1.22	5.22	6.15
CN35	−81.363	13.376	1.16	4.32	−0.36	0.89	0.71	3.07	4.47
HAVA	−82.395	23.121	−3.29	2.72	−5.97	1.99	1.79	7.49	4.27
CARD	−81.210	23.029	−3.34	2.31	1.04	1.80	1.62	6.96	4.06
CN13	−74.534	24.065	−3.52	−1.80	−3.80	0.80	0.70	2.91	3.95
UNPM	−86.868	20.869	−3.50	1.76	−0.71	0.60	0.52	2.15	3.92
TGMX	−86.867	20.868	−3.28	2.10	−1.74	1.09	0.93	3.99	3.89
SAN0	−81.716	12.581	1.12	3.37	−1.57	0.92	0.76	3.21	3.55
MTNT	−80.907	25.866	−2.55	0.38	−5.53	0.76	0.68	2.88	2.58
ZMA1	−80.319	25.825	−2.4	0.09	−2.89	0.96	0.88	3.70	2.40
CN53	−72.254	21.783	−2.02	0.85	−1.86	0.86	0.74	3.10	2.19
CN37	−75.263	10.793	−1.6	0.97	−7.43	0.72	0.60	2.35	1.87
CN27	−69.940	19.667	−1.58	−0.25	−3.91	0.97	0.82	3.57	1.60
JME2	−72.538	18.235	1.19	−0.19	0.77	0.96	0.81	3.54	1.21
CN14	−73.678	20.975	−0.94	−0.64	−4.60	0.82	0.70	2.96	1.14
RDF2	−70.680	19.452	−1.02	0.43	−3.18	1.04	0.88	3.76	1.11
CRLR	−68.917	18.449	−1.00	−0.29	−2.32	1.04	0.87	3.73	1.04
CN06	−70.656	18.790	0.78	0.63	−2.60	0.92	0.76	3.38	1.27
RDMA	−71.077	19.539	−0.56	−0.81	−2.70	0.94	0.79	3.34	0.98
RDLT	−69.547	19.307	−0.56	−0.81	−2.70	0.94	0.79	3.34	0.98
CN23	−88.779	17.261	−0.37	0.81	0.35	1.46	1.15	5.72	0.89
RDBA	−70.328	18.277	0.23	−0.86	−2.58	1.08	0.9	3.88	0.89
RDAZ	−70.716	18.446	−0.54	0.53	−1.50	1.02	0.86	3.72	0.77
SROD	−71.341	19.475	0.48	0.54	−3.74	1.06	0.9	3.98	0.72
SPED	−69.306	18.461	−0.23	−0.63	−2.81	1.00	0.83	3.64	0.67
CRSE	−69.044	18.768	0.37	0.49	−5.37	1.09	0.91	3.95	0.61
RDMS	−69.041	18.980	−0.42	0.23	−2.80	1.03	0.87	3.70	0.48
RDSF	−70.247	19.286	−0.35	0.26	−1.43	0.99	0.83	3.51	0.44
CN05	−68.359	18.564	−0.30	0.22	−1.78	0.97	0.81	3.47	0.37
RDMC	−71.639	19.849	0.18	−0.29	1.53	1.08	0.92	3.89	0.34
RDHI	−68.718	18.598	−0.25	−0.10	0.23	1.03	0.86	3.63	0.27
RDSD	−69.911	18.461	−0.08	0.01	−3.38	0.64	0.55	2.2	0.08
VPOL	−74.861	10.794	−0.03	−0.04	0.03	0.38	0.30	1.28	0.05

Coseismic displacements at regional continuous GPS sites. Displacements and standard deviations are in millimeters. The site locations can be found on Figure 6.